nature energy

Article

https://doi.org/10.1038/s41560-026-02035-4

Reactive CO_2 capture via controlled amine speciation in non-aqueous electrolytes

Received: 12 July 2024

Accepted: 10 March 2026

Check for updates

Reginaldo J. Gomes[1], Jianping Li[2], Jiayi Xu[3,4], Bidushi Sarkar[1], Matin Mohebi[1], Joshua Gabriel[5], Tony Mathew[2], Ishaan Roy[1], Noah Paulson[5], Cong Liu[3,4], Chukwunwike O. Iloeje[2,4] & Chibueze V. Amanchukwu[1,3]

Current efforts to integrate CO_2 capture and electrochemical conversion are often performed under aqueous conditions, resulting in undesired hydrogen evolution and reliance on precious metal catalysts and pure CO_2 streams. Here we explore reactive capture in aprotic media. By shifting the amine–CO_2 adduct speciation to carbamic acid (instead of carbamate) in dimethyl sulfoxide, we increased CO_2 uptake threefold compared with an aqueous medium, suppressing hydrogen evolution and supporting a 78% Faradaic efficiency towards CO over an earth-abundant zinc catalyst. Under simulated high-oxygen-content flue gas (17% CO_2, 17% O_2, 66% N_2), we also obtained up to 43% CO Faradaic efficiency over multiple capture–conversion cycles. Our findings showcase the confluence of reactant speciation, electrolyte composition and electrocatalyst design in enabling selective and active electrochemical transformations.

Integrating carbon capture and use, also referred to as reactive CO_2 capture (RCC), offers a pathway to decrease emissions from industrial point sources while generating value-added fuels and chemicals[1]. Major manufacturing and power sectors emit flue gases containing 10–20% CO_2 together with nitrogen, oxygen and minor contaminants[2]. Conventionally, CO_2 is captured using aqueous amine solutions and subsequently released in a thermal regenerator operating at temperatures up to 150 °C[3]. This regeneration step is the most energy-intensive component of the capture process[3]. In contrast, in a RCC unit, the captured species is directly converted without thermal desorption, potentially eliminating separate purification and pressurization steps and lowering overall energy demand[1,4].

Electrochemical approaches to reactive capture are attractive because they are modular and can operate at ambient temperature and pressure. Most electrochemical RCC systems rely on aqueous amine electrolytes[5–7], where CO_2 reacts with primary or secondary amines (for example, monoethanolamine (MEA)) to form carbamate and ammonium species[8]. However, formation of the amine–CO_2 adduct in water is fundamentally limited by the 2:1 amine-to-CO_2 stoichiometry and the competing equilibria with ammonium, bicarbonate and carbonate ions. In addition, the plethora of proton sources (for example, H_2O, HCO_3^-, $R–NH_3^+$) favours competing side reactions such as hydrogen evolution reaction (HER)[6,9,10], lowering selectivity towards CO_2 conversion. Furthermore, when oxygen is present in the feed (as is typical in flue gas streams), undesired oxygen reduction reaction predominates[11–13]. Even when alkali cations are introduced to modify the electrochemical double layer to facilitate carbamate reduction[6], CO formation remains sensitive to CO_2 partial pressure[14] and often requires noble metal catalysts (for example, Ag) and oxygen-free feeds[6,14].

The use of aprotic solvents offers a viable strategy to increase RCC selectivity by tuning the amine–CO_2 adduct speciation and limiting availability of proton donors[15–17]. In polar organic solvents such as dimethyl sulfoxide (DMSO), amine–CO_2 adducts speciate towards carbamic acid and its zwitterion analogue rather than carbamate–ammonium ion pairs[18]. This pathway requires only one amine per CO_2 molecule, doubling the theoretical CO_2 uptake relative to aqueous medium. As neutral species, carbamic acid may also experience reduced electrostatic repulsion at negatively biased electrodes compared with anionic carbamate. Moreover, DMSO can decrease the electrochemical activity of water[17], proton[19] and O_2[20] towards undesired HER and oxygen reduction

[1]Pritzker School of Molecular Engineering, The University of Chicago, Chicago, IL, USA. [2]Energy Systems and Infrastructure Analysis Division, Argonne National Laboratory, Lemont, IL, USA. [3]Chemical Sciences and Engineering Division, Argonne National Laboratory, Lemont, IL, USA. [4]Consortium for Advanced Science and Engineering (CASE), Pritzker School of Molecular Engineering, The University of Chicago, Chicago, IL, USA. [5]Data Science and Learning and Applied Materials Divisions, Argonne National Laboratory, Lemont, IL, USA. e-mail: chibueze@uchicago.edu

https://doi.org/10.1038/s41560-026-02035-4

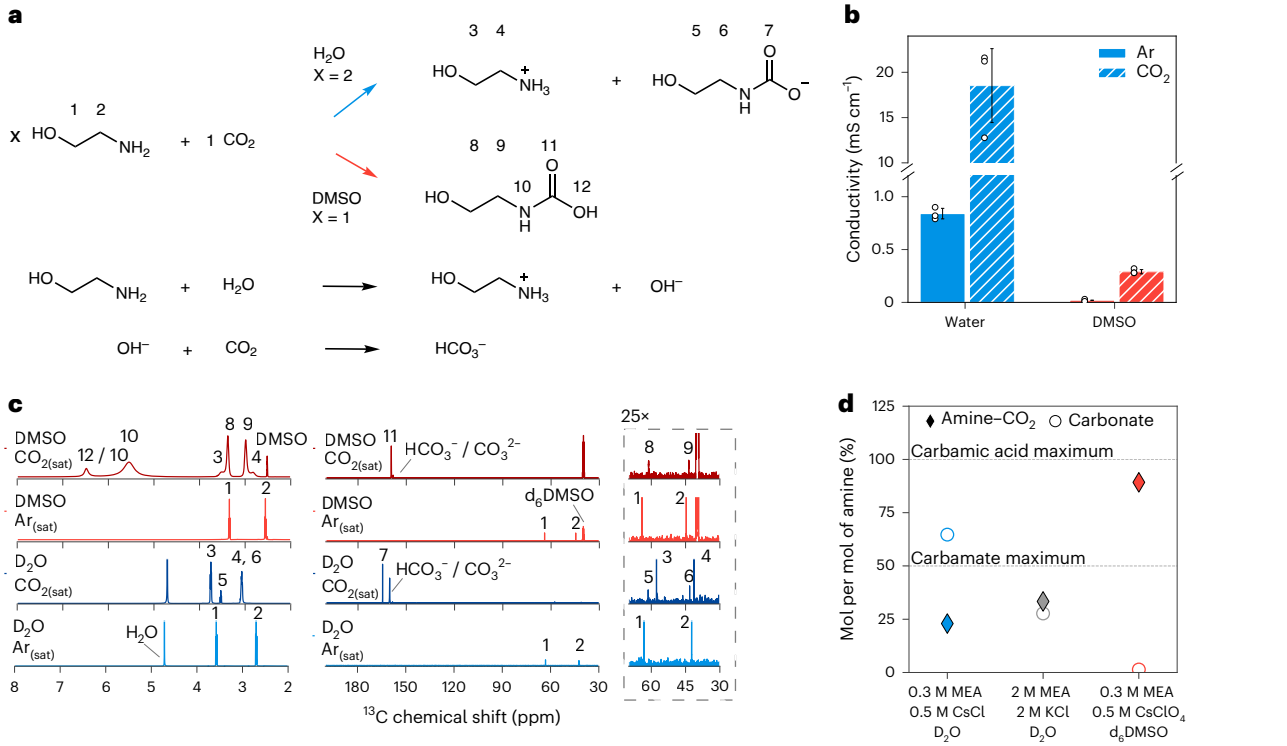

Fig. 1 | Amine–CO_2 speciation. a, Summary of amine and CO_2 speciation in water and DMSO. **b**, Conductivity measurements of Ar and CO_2 saturated solutions containing 0.3 M MEA in water and DMSO. **c**, ^{1}H NMR and ^{13}C NMR chemical shifts for Ar and $^{13}CO_2$-saturated solutions containing 0.3 M MEA with 0.5 M CsCl in D_2O or 0.5 M $CsClO_4$ in d_6DMSO. $^{13}CO_2$-saturated solutions were initially purged with Ar for the removal of soluble CO_2. Nomenclature for identification of ^{1}H and ^{13}C NMR peaks are shown in **a**. Atom numbering in **a** is provided solely to facilitate assignment of the corresponding ^{1}H and ^{13}C NMR peaks. **d**, $^{13}CO_2$ uptake per mol of amine in different electrolyte compositions. Data in **b** are presented as mean values, while dots represent individual measurements (n = 3) and bars show mean ± s.d.

reaction. We therefore propose that promoting carbamic acid formation in a non-aqueous electrolyte will simultaneously increase effective CO_2 uptake and mitigate competing reaction, enabling CO_2 conversion over non-noble metal catalysts and under industrially relevant CO_2 partial pressures and oxygen contents.

Here we investigate RCC using MEA in DMSO. We quantify CO_2 uptake, characterize amine–CO_2 speciation and stability, and show that CO formation during RCC is possible even with an earth-abundant Zn-based catalyst. Replacing water with DMSO increases CO_2 uptake threefold and suppresses undesired HER. Furthermore, CO Faradaic efficiency (FE) reaches up to 78% in the non-aqueous electrolyte, with Zn exhibiting activity comparable to or exceeding Ag under identical conditions. Density functional theory (DFT) calculations indicate a lower limiting potential for CO formation on Zn, consistent with experiment. Under simulated flue gas conditions with high oxygen content (HOC) and lower CO_2 partial pressures, the system sustains CO Faradaic efficiencies up to 43% over repeated capture–conversion cycles. These findings demonstrate that electrolyte-controlled amine–CO_2 speciation enhances capture capacity and selectivity under industrially relevant conditions using earth-abundant catalysts.

Amine–CO_2 speciation

We first examined how solvent influences amine–CO_2 speciation. In water, we may expect CO_2 reacts with two MEA molecules to form carbamate and ammonium species[8], as illustrated in Fig. 1a. Due to its basicity, MEA can further promote the formation of hydroxide, bicarbonate and carbonate ions. In contrast, in DMSO the reaction predominantly yields neutral carbamic acid[18]. This difference in speciation is reflected in the solution conductivity. As shown in Fig. 1b, on CO_2 addition the conductivity of a 0.3 M MEA aqueous solution increases by nearly 20 mS cm^{-1}, whereas in DMSO the increase is only 0.3 mS cm^{-1}, consistent with minimal formation of ionic species in the non-aqueous medium.

We next investigated the effect of caesium salts, as large alkali cations have been shown to promote carbamic acid speciation in DMSO[21,22] and suppressing HER in aqueous systems[6]. Figure 1c presents the ^{1}H NMR spectra of Ar-saturated and $^{13}CO_2$-saturated MEA solutions in D_2O and deuterated DMSO (d_6DMSO) containing 0.5 M Cs salts (either CsCl or $CsClO_4$). The $^{13}CO_2$-saturated solutions were purged with argon to remove dissolved CO_2 (Supplementary Fig. 1). In Ar-saturated solutions, two triplets at approximately 3.5 ppm and 2.6 ppm are observed in both solvents, corresponding to MEA. On $^{13}CO_2$ addition, four new peaks appear in D_2O, consistent with formation of carbamate and ammonium species. In d_6DMSO, the 2 new peaks at 3.4 ppm and 3.0 ppm are assigned to the –CH protons of carbamic acid, while broad resonances at 6.5 ppm and 5.6 ppm arise from rapid proton exchange involving amide, ammonium and hydroxyl groups[18,23]. Minor signals attributable to ammonium species are also detected in d_6DMSO, however, carbamic acid remains the dominant adduct.

We also used ^{13}C NMR spectroscopy to identify carbon-containing species not resolved in the ^{1}H spectra. The peaks shown in Fig. 1c were assigned on the basis of previous reports[8,18] and two-dimensional heteronuclear NMR analysis (Supplementary Fig. 2). In aqueous solution, distinct peaks at 165 ppm and 158 ppm are assigned to carbamate and to rapidly exchanging bicarbonate and/or carbonate species[8], respectively. In DMSO, peaks at 158.5 ppm correspond to carbamic acid[18] while the 158 ppm peaks correspond to minor bicarbonate and/or carbonate formation[24].

The integration of the ^{13}C signals (Supplementary Fig. 3) was then used to estimate the total CO_2 loading relative to the initial amount of amine. As shown in Fig. 1d, at 0.3 M in water, only 15% of MEA is converted to carbamate. Increasing the amine and salt concentration

https://doi.org/10.1038/s41560-026-02035-4

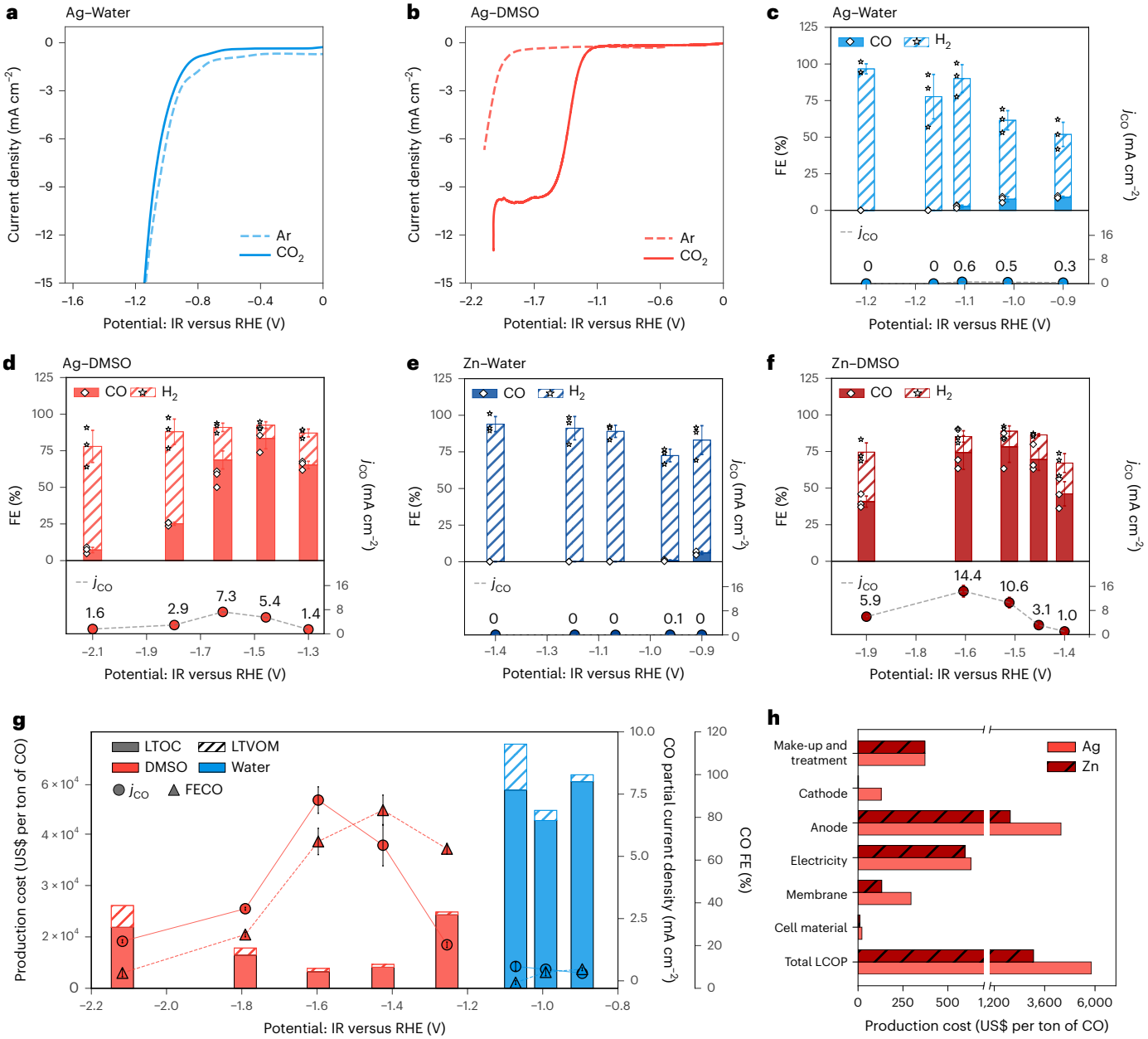

Fig. 2 | Electrochemical analysis. a,**b**, Linear sweep voltammograms at 50 mV s^{-1} over an Ag disc electrode for Ar and CO_2 saturated solutions containing 0.3 M MEA and 0.5 M CsCl in water (**a**) and 0.5 M $CsClO_4$ in DMSO (**b**). **c**–**f**, Product distribution analysis using an H-cell setup with Ar as a carrier gas at 5 sccm for CO_2 saturated solutions containing 0.3 M MEA and 0.5 M Cs salts in water (**c**) and DMSO (**d**) over a Ag disc electrode and water (**e**) and DMSO (**f**) over a Zn disc electrode. All CO_2-saturated solutions (~15 ml) were purged with Ar at 5 sccm for 5 min to remove dissolved CO_2 before electrochemistry. **g**, LTOC and LTVOM for CO production in water and DMSO over Ag catalysts under electrochemical conditions present in **c** and **d**. **h**, CO production cost breakdown over Ag and Zn catalysts in DMSO under electrochemical conditions presented in **d** and **f** at −1.5 V. Data in **c**–**f** are presented as means, while dots represent individual measurements ($n = 3$) and bars show mean ± s.d. IR, infrared; RHE, reversible hydrogen electrode.

to 2 M, used here as literature benchmarks[6,14], raises carbamate conversion to 31%. However, substantial bicarbonate or carbonate formation persists, accounting for approximately 64% and 28% of carbon-containing species at 0.3 M and 2 M MEA, respectively. In contrast, in DMSO approximately 87% of MEA converts to carbamic acid with only ~2% bicarbonate or carbonate formation. Overall, CO_2 uptake per mole of amine in the form of a reducible amine–CO_2 adduct is nearly three times higher in DMSO than in water, with minimal carbonate loss.

Electrolyte effects on amine–CO_2 reduction

The role of amine–CO_2 speciation in modulating electrochemical selectivity was probed. Figure 2a,b presents the voltammograms obtained from the water and DMSO electrolytes before and after saturation with CO_2. The cathodic potential in the non-aqueous medium was referenced against the reversible hydrogen electrode[25], further discussed in Supplementary Note 1 and Supplementary Fig. 4. We also purged the electrolytes with Ar to eliminate any dissolved CO_2. In water, we only observed a single cathodic feature at −0.9 V versus the reversible hydrogen electrode for both Ar and CO_2 saturated solutions. In DMSO, we observed a cathodic feature at −1.9 V, which we ascribed to amine reduction or electrolyte degradation. However, when CO_2 was added, we observe a second cathodic feature at −1.2 V that remained diffusion-limited around −10 mA cm^{-2} until electrolyte reduction and/or degradation took place. This diffusion-limited current shifts to more

https://doi.org/10.1038/s41560-026-02035-4

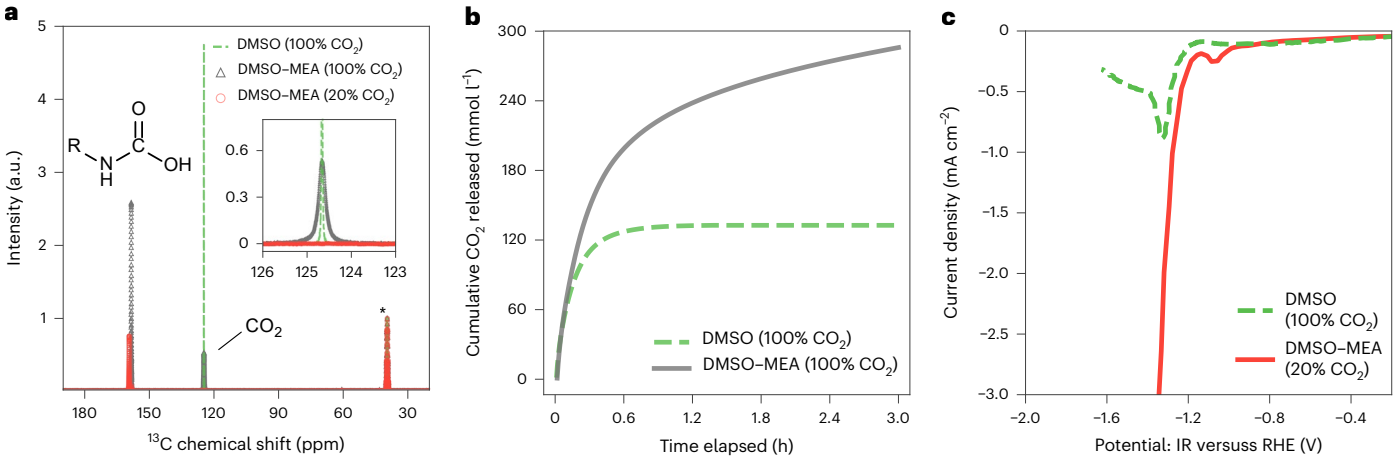

Fig. 3 | Role of the amine–CO_2 adduct. a, ^{13}C NMR spectra of solutions containing 0.5 M $CsClO_4$ (green) and 0.3 M MEA in d_6DMSO saturated with either 100% $^{13}CO_2$ (grey) or 20% $^{13}CO_2$/80% Ar (red). All data were normalized against the d_6DMSO peak (*). **b**, CO_2 displacement test of DMSO solutions saturated with 100% CO_2. Ar at 10 sccm was used as a carrier gas. **c**, Linear sweep voltammograms over an Ag electrode at 5 mV s^{-1} of DMSO CO_2 saturated solutions containing either 0.5 M $CsClO_4$ saturated with 100% CO_2 or 0.5 M $CsClO_4$ and 0.3 M MEA saturated with 20% CO_2/80% Ar equilibrated over 1 h to minimize the amount of dissolved CO_2 in the solution.

negative values as the MEA concentration increases (Supplementary Fig. 5), suggesting that the amine–CO_2 adduct may act as the limiting reactant in the system.

Product distribution analysis at different potentials may offer insights on how electrolyte composition affects selectivity. In water, the maximum CO FE is 9% at −1.0 V, with CO partial current density below 1 mA cm^{-2} even at −1.3 V (Fig. 2c). Similar CO FE between 9%[9] and 19% (ref. 14) have been reported under comparable conditions. In contrast, in DMSO the CO FE reaches 83% at −1.45 V (Fig. 2d), with a maximum CO partial current density of 7.3 mA cm^{-2} at −1.6 V. The higher CO selectivity in DMSO is consistent with greater CO_2 loading and reduced availability of proton donors such as H_2O, HCO_3^- and RNH_3^+ shown in our NMR results. Moreover, it has been shown that DMSO can form strong hydrogen bond networks, decreasing both proton and water activity towards HER[17,19].

Since the observed increase in CO activity and selectivity is fundamentally influenced by the electrolyte composition, we proposed that comparable outcomes could be achieved using an earth-abundant electrode. Polycrystalline Zn is one of the cheapest metals (Supplementary Table 1) and presents superior selectivity towards CO for CO_2 reduction (CO_2R) in both aqueous and non-aqueous medium[26–29]. Figure 2e shows that Zn performed poorly in water, with CO FE and partial current density values not exceeding 5% and 1 mA cm^{-2}, respectively. In contrast, Fig. 2f shows CO FE values up to 78% in DMSO at −1.5 V, with a j_{CO} reaching 14.4 mA cm^{-2} at more negative potentials. These results show a stark increase in both CO activity and selectivity for amine–CO_2 reduction over non-noble metal catalysts at room temperature when shifting from water to DMSO electrolyte.

We implemented a techno-economic analysis (TEA) model to evaluate the competitiveness of amine–CO_2 reduction in non-aqueous electrolyte. Key input parameters and cost breakdowns are summarized in Supplementary Table 2, Supplementary Figs. 6 and 7 and Supplementary Note 2. Together, these terms define the levelized cost of production for CO within the constraints of a technology readiness level 1 system. At this early stage, the TEA does not represent an engineering design, nor does it capture higher-technology readiness-level requirements such as large-scale balance-of-plant integration, compression and recycle loops, long-term stability or detailed separations. Nevertheless, it serves as a bounded, physics-based comparison across experimental conditions from both aqueous and non-aqueous systems.

Figure 2g shows a substantial cost reduction of nearly 89% for CO_2 reduction over silver catalyst when operating the cell in DMSO at −1.5 V, compared with water at −0.99 V. The major contributors to this cost reduction are the higher CO FE and partial current density in DMSO, which are one order of magnitude greater than in water. We expanded our TEA to evaluate the impact of replacing silver with a non-noble metal Zn catalyst. Figure 2h indicates that adopting zinc yields a substantial cost reduction relative to silver. A fraction of this improvement originates from lower catalyst cost, while the dominant contribution arises from higher CO activity with zinc, which decreases electricity use, solvent make-up and hardware requirements (Supplementary Fig. 7a–c). The influence of engineering factors such as membrane lifetime and electricity price is summarized in Supplementary Fig. 8. Preliminary two-dimensional sweep analysis further indicates that achieving current densities above 100 mA cm^{-2} and using alternative anodes such as nickel can expand the operating region in which integrated CO_2 capture and conversion becomes economically competitive (Supplementary Fig. 9).

The role of the amine–CO_2 adduct

It is an ongoing debate whether the amine–CO_2 adduct can undergo direct reduction or if CO_2 will first be released and then reduced to CO[9,14]. To elucidate the role of amine–CO_2 adduct during CO formation in DMSO, we first investigated the role of MEA and CO_2 partial pressure in CO_2 speciation. The ^{13}C NMR spectra in Fig. 3a shows a single peak at 125 ppm in the absence of MEA, corresponding to dissolved CO_2. On the addition of MEA, most of the CO_2 is converted to carbamic acid. As the CO_2 partial pressure decreases to 20%, the carbamic acid peak intensity diminishes and no appreciable amount of dissolved CO_2 is detected. We selected a CO_2 partial pressure of 20% as a representative condition for the product distribution analysis shown in Fig. 2d (Supplementary Fig. 10). Our observations indicate that carbamic acid serves as a reservoir, dynamically releasing CO_2 as it is either consumed during electrochemical reduction or displaced during purging with inert gas.

To verify whether the amine–CO_2 adduct (rather than dissolved CO_2) serves as the primary CO_2 reservoir, we conducted a displacement test to quantify the total CO_2 loading with and without MEA (cell illustration in Supplementary Fig. 11). As shown in Fig. 3b, the CO_2 loading in DMSO without amine is 130 ± 1 mmol l^{-1}, consistent with reported literature values[30]. In the presence of MEA, the CO_2 loading increases to 289 ± 5 mmol l^{-1}, closely aligning with the initial amine concentration (300 mM). These findings corroborate the ^{13}C NMR results, confirming that CO_2 is predominantly present as an amine–CO_2 adduct and is released on purging the system with an inert gas.

https://doi.org/10.1038/s41560-026-02035-4

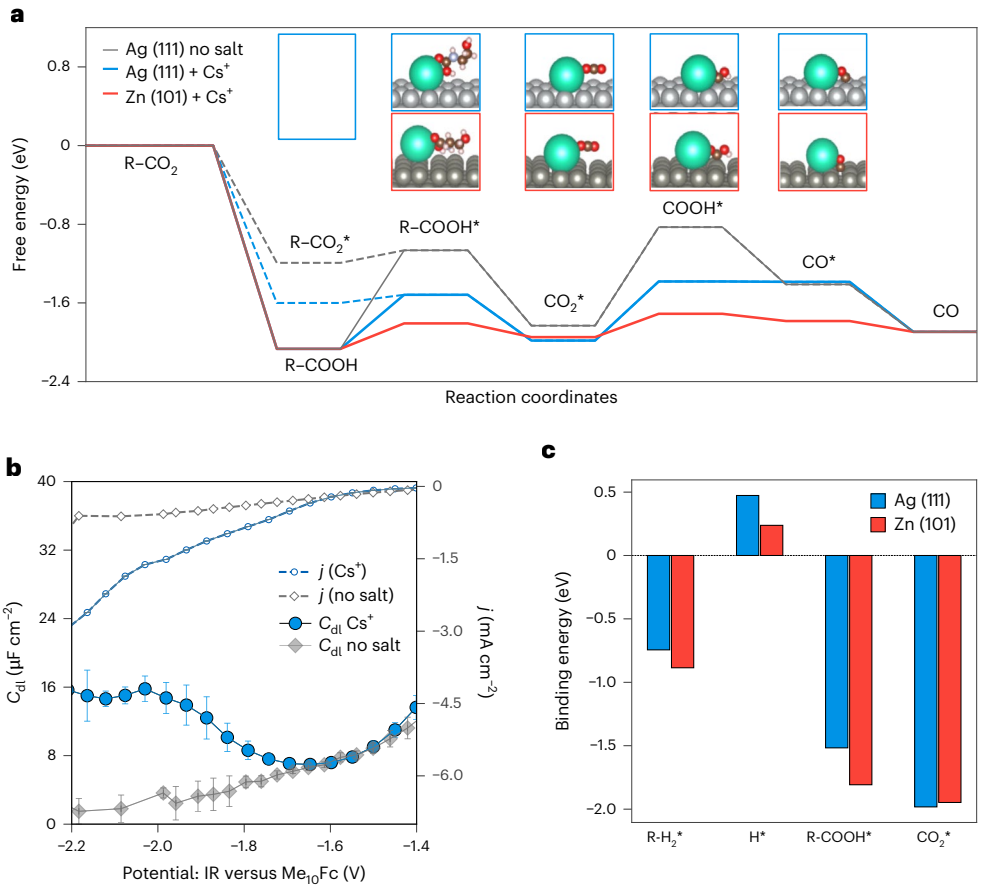

Fig. 4 | Insights into catalytic activity and selectivity. a, Free energy diagram for the amine–CO_2 reduction over Ag (111) and Zn (101) catalysts in the presence and absence of Cs^+. Pathway starting with carbamate adsorption over an Ag (111) facet is represented in dashed lines. **b**, Double-layer capacitance (C_{dl}) and current density values (j) averaged over 1 min during electrochemical impedance spectroscopy experiments over a Ag disc catalyst of CO_2 saturated solution containing 0.3 M MEA with and without 0.5 M $CsClO_4$. The two non-aqueous systems were compared against the internal standard decamethylferrocene ($Me_{10}Fc$). **c**, Binding energy for potential proton donors for HER and carbon sources for CO formation over an Ag (111) and Zn (101) facets in the presence of Cs^+. 'R–' equals $HOCH_2CH_2NH$–. Data in **b** are presented as mean values, while dots represent individual measurements ($n = 3$) and bars show mean ± s.d.

Finally, we probed whether an electrochemical process can drive CO_2 release and subsequent reduction. In the absence of amine (Fig. 3c), CO_2 reduction takes place around −1.25 V versus the reversible hydrogen electrode in DMSO. However, the electrode becomes inactive at more negative potentials due to the formation of poorly soluble caesium bicarbonates or carbonates[24,31]. In contrast, when MEA is added, the onset potential for amine–CO_2 reduction remains nearly the same, but electrode inactivation is mitigated. These findings suggest that CO_2 is the active species for CO formation, consistent with previous studies in aqueous systems[9,14]. However, the reaction is mediated by the formation of the amine–CO_2 adduct, which in equilibrium with CO_2 ($CO_2 + R\text{–}NH_2 \rightleftharpoons R\text{–}NHCO_2H$) outcompetes the formation of insoluble bicarbonates ($CO_2 + OH^- \rightleftharpoons HCO_3^-$) that would otherwise inactivate the electrode.

Amine–CO_2 reduction activity and selectivity

We carried out DFT simulations to investigate the amine–CO_2 reduction activity and selectivity. Calculations were performed over Ag (111) and Zn (101), which were the dominant electrode facets before and after electrolysis (Supplementary Fig. 8). Further details about DFT calculations can be found in Supplementary Note 3. Our results over the Ag (111) in Fig. 4a show that the carbamic acid formation in the liquid phase presents more negative free energy values than carbamate adsorption (dashed grey line) by −0.9 eV. Thus, carbamic acid is more likely to act as the amine–CO_2 shuttle than its carbamate form. We also observed that the release of CO_2 presents −0.77 eV over the Ag electrode, indicating that CO_2 is most likely the active species for the amine–CO_2 reduction, in agreement with our experimental results. The proton-coupled electron transfer reaction that leads to the formation of COOH* is uphill by 0.99 eV. This step is followed by thermodynamically favoured CO* formation and CO desorption steps.

The free energy diagram in Fig. 4a shows that Cs^+ (solid blue line) strengthens carbamic acid binding on Ag by 0.45 eV and lowers the formation energy of COOH* by 0.55 eV, facilitating CO_2 reduction. To probe the role of Cs^+ in DMSO, we quantified the electrochemical double-layer capacitance (C_{dl}) with and without supporting electrolyte. The circuit model and fitting parameters are provided in Supplementary Fig. 13. Figure 4b shows that, in the presence of Cs^+, C_{dl} increases to ~16 μF cm^{-2} from −1.8 V to −2.2 V versus $Me_{10}Fc$, where amine–CO_2 reduction takes place. Without salt, C_{dl} remains between 2 μF cm^{-2} and 6 μF cm^{-2}, suggesting that Cs^+ ions increase local dielectric constant and favours a more compact double layer that may enhance CO activity, as suggested by DFT. In the absence of supporting ions, zwitterionic species ($R\text{–}NH_2^+CO_2^-$) and ammonium ions leads to a thicker double layer and lower CO selectivity (CO FE values for different Cs^+ concentrations are shown in Supplementary Fig. 14).

Our experiments also have shown that Zn exhibits higher activity for amine–CO_2 reduction than Ag. From the free energy diagrams in Fig. 4a, the limiting potential for *COOH formation on Zn (101) is 0.24 eV, markedly lower than 0.61 eV on Ag. A similar Cs^+ effect is

https://doi.org/10.1038/s41560-026-02035-4

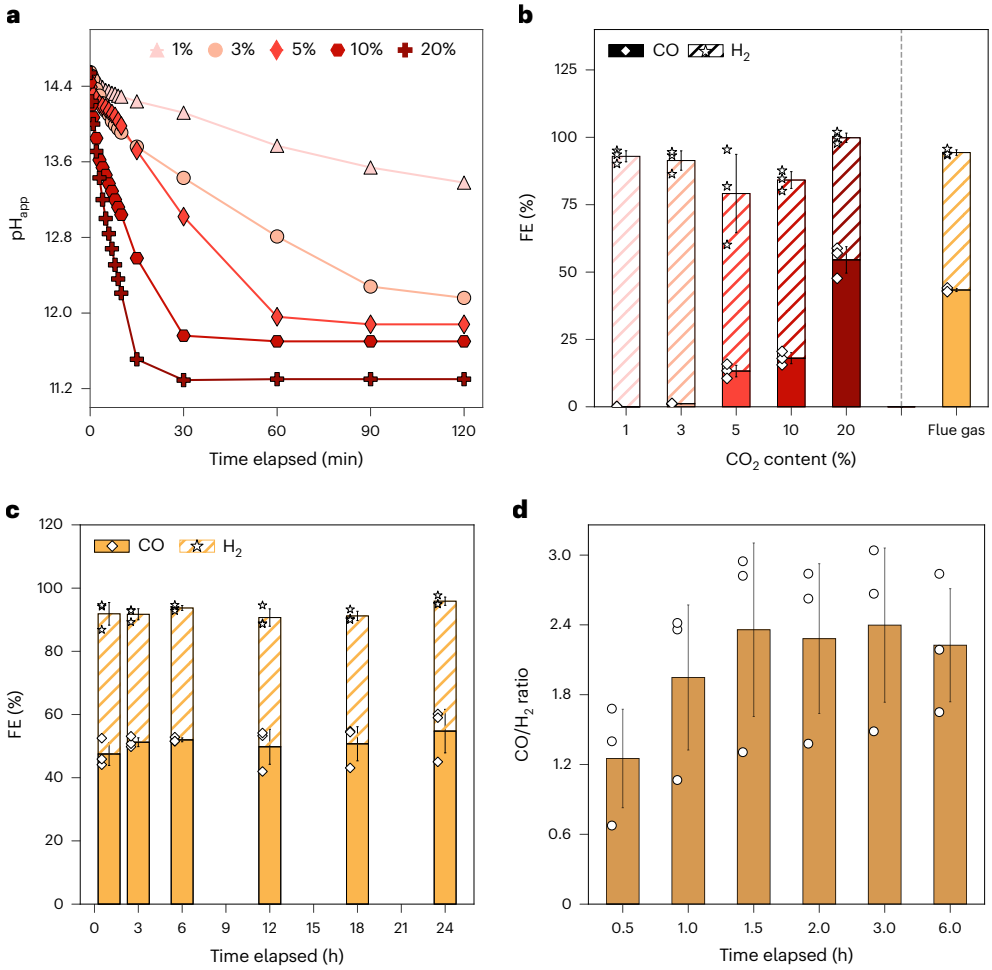

Fig. 5 | Effect of CO_2 composition on product selectivity. a, Apparent pH of solutions containing 0.3 M MEA and 0.5 M of $CsClO_4$ in d_6DMSO fed with different CO_2/Ar compositions at 10 sccm. **b**, Galvanostatic product distribution analysis for different CO_2 stream compositions as carrier gas at 20 sccm for solutions containing 0.3 M MEA and 0.5 M $CsClO_4$ in DMSO over a Zn electrode at −10 mA cm^{-2}. Flue gas contains 16% CO_2, 3% O_2 and 81% N_2. **c**, Galvanostatic product distribution analysis for 0.3 M MEA and 0.5 M $CsClO_4$ in DMSO over a Zn electrode at −10 mA cm^{-2} over 24 h under constant flue gas flow of simulated flue gas at 20 sccm. **d**, Product distribution analysis of 0.5 M $CsClO_4$ and 0.3 M MEA in DMSO saturated with simulated flue gas over a Zn electrode at −10 mA cm^{-2} under quiescent conditions over 6 h (-20 C charge passed). Data in **b**–**d** are presented as mean values, while dots represent individual measurements ($n = 3$) and bars show mean ± s.d.

observed for Zn (101) (Supplementary Fig. 15). Enhanced Zn activity for CO formation in non-aqueous CO_2 reduction has also been reported; whereas in aqueous systems Zn shows slightly lower activity than Ag[29].

To rationalize the high CO selectivity in DMSO, we extended DFT calculations to possible HER proton donors. Figure 4c compares the binding energies of H^+ and R–NH_3^+ with those of carbamic acid and CO_2. In the absence of water, H^+ may arise from carbamic acid ionization, while R–NH_3^+ forms via reaction with unconverted amine. The full HER pathway and Cs^+ effects are shown in Supplementary Fig. 16. Both carbamic acid and CO_2 bind more strongly to Zn and Ag than H^+ or R–NH_3^+, supporting selective CO formation in DMSO. In aqueous media, higher concentrations of R–NH_3^+, water and HCO_3^- (not captured in our DFT) may promote substantial HER.

Operation under oxygen-rich and low CO_2 partial pressure environment

Industrial flue gases typically contain 5–20% CO_2[2]. We therefore examined how CO_2 content influences amine–CO_2 speciation and electroreduction in DMSO. Figure 5a shows the apparent pH (pH_{app}) of MEA solution in DMSO under varying CO_2/Ar mixtures. Increasing CO_2 fraction produces a more acidic pH plateau, consistent with equilibrium dependence on CO_2 partial pressure. ^{1}H NMR analysis after gas purging (Supplementary Fig. 17) confirms increased conversion of MEA to carbamic acid at higher CO_2 content. We then analysed product distribution over Zn to assess CO formation under varying gas compositions. CO_2/Ar mixtures were used to avoid speciation shifts caused by inert purging (Supplementary Fig. 5b). Figure 5b shows substantial CO production even at 20% and 10% CO_2, corresponding to CO Faradaic efficiencies of 54% and 18%, respectively.

Collectively, spectroscopic and product analyses confirm selective capture and conversion of the amine–CO_2 adduct in DMSO for CO_2 concentrations as low as 10%. We therefore evaluated performance under simulated flue gas (17% CO_2, 3% O_2, 81% N_2). As shown in Fig. 5b, the system achieves up to 43% CO FE under this condition. A 24 h stability test (Fig. 5c) shows sustained CO formation with FE near 58% at 24 h and minimal oxygen reduction losses (unaccounted FE < 5%). No carbamic acid crossover (Supplementary Fig. 18) or electrolyte degradation was observed. The small unaccounted FE may also arise from formic acid formation (Supplementary Fig. 19). The gradual increase in CO FE probably reflects slow carbamic acid equilibration in DMSO, which can require up to 72 hours[21,32].

Experiments conducted under quiescent conditions (that is, without the flow of a carrier gas) revealed higher production of CO compared with H_2, with a ratio of approximately 2:1 over 6 hours of electrolysis (Fig. 5d). These findings along with a change in carbamic acid speciation (Supplementary Fig. 20) suggest that CO_2 is primarily

https://doi.org/10.1038/s41560-026-02035-4

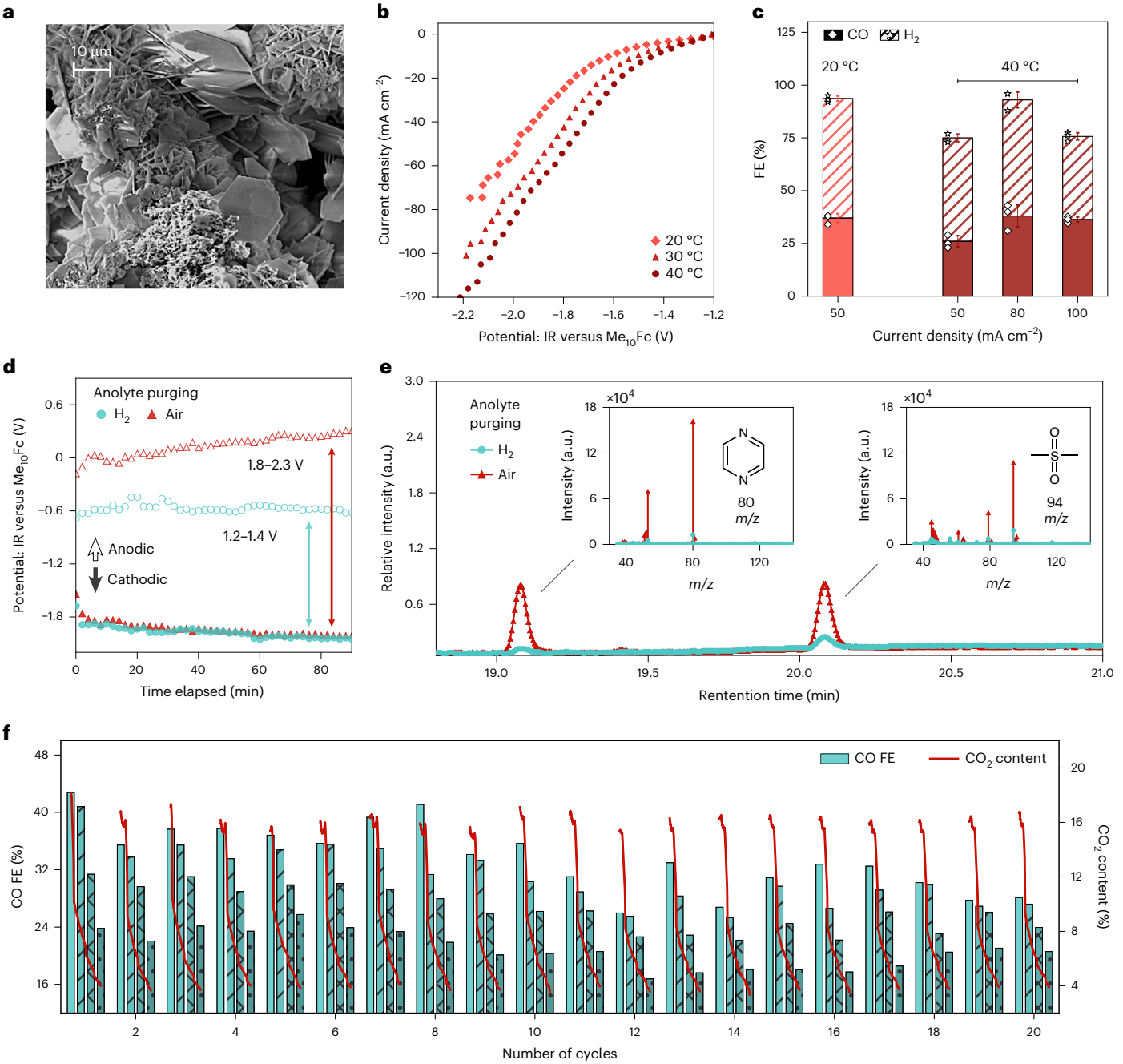

Fig. 6 | Amine–CO_2 reduction under industrially relevant conditions. **a**, Scanning electron microscopy image of the electrodeposited Zn particles over a stainless-steel cloth. **b**, Linear sweep voltammograms at 50 mV s^{-1} over a Zn cloth electrode of DMSO solution containing 0.3 M MEA and 0.5 M $CsClO_4$ saturated with HOC-FG (17% CO_2, 17% O_2, 66% N_2) at different temperatures. Experiments were conducted in an H-cell setup and Pt wire was used as a counter electrode. **c**, Galvanostatic product distribution analysis for the solution in **b** under different current densities and temperatures. HOC-FG at 20 sccm was used as a carrier gas. **d**, Galvanostatic test at 100 mA cm^{-2} and 40 °C in a three-electrode H-cell setup for solutions in **b**. Anolyte was purged with either H_2 or Air at 20 sccm and approximately 1.5 C ml^{-1} was passed during the test. A porous palladium membrane was used as a counter electrode and Zn cloth was used as a working electrode. **e**, GC–MS analysis of the anolyte solutions in **d**. **f**, Accelerated recycling performance of the 0.3 MEA and 0.5 M $CsClO_4$ electrolyte at a constant applied current of 100 mA cm^{-2} over Zn cloth at 40 °C in an H-cell configuration, and H_2 at 20 sccm purged in the anolyte. Each cycle comprises a step for catholyte saturation with HOC-FG, followed by purging with synthetic air (20% O_2, 80% N_2) at 10 sccm. Data in **c** are presented as mean values, while dots represent individual measurements ($n = 3$) and bars show mean ± s.d.

supplied by the amine–CO_2 adduct as the reaction progresses. The high CO selectivity observed under quiescent conditions indicates a promising strategy to minimize potential CO_2 losses associated with the reversible amine–CO_2 equilibrium and the purging of carrier gas.

Next, we engineered both the electrode and the electrolyte to enhance the amine–CO_2 reduction current density and improve electrolyte stability under higher oxygen-content conditions. A porous Zn electrode was fabricated by electrodepositing Zn microparticles and nanoparticles onto a stainless-steel cloth. As shown in Fig. 6a, the Zn deposits exhibit hexagonal shapes, offering a higher surface area compared with a flat disc architecture of the same geometric area (additional images in Supplementary Fig. 21a–f). The geometric surface area was used here as others have done for a porous structure[6,33,34]. The electrochemical performance of the new porous electrode was

https://doi.org/10.1038/s41560-026-02035-4

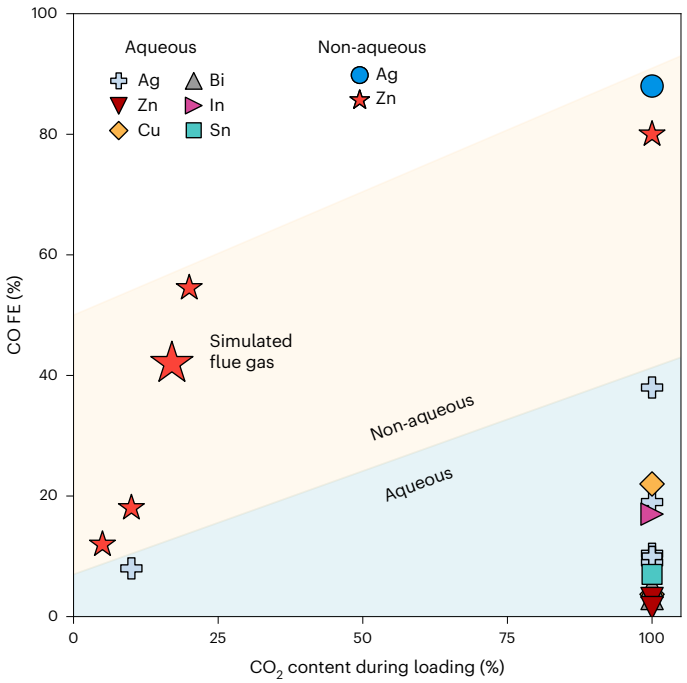

Fig. 7 | Electrochemical performances of amine–CO_2 reduction. Comparative performance of different reactive capture systems using MEA at room temperature. The shaded regions labelled 'Aqueous' and 'Non-aqueous' represent literature-reported performance for systems operating with MEA solution in water and any organic solvent, respectively. The literature data used to construct these regions are summarized in Supplementary Table 6. Simulated flue gas refers to HOC-FG (17% CO_2, 17% O_2, 66% N_2).

evaluated in a DMSO-based electrolyte saturated with a HOC-flue gas (HOC-FG) mixture composed of 17% CO_2, 17% O_2 and 66% N_2. HOC introduces two challenges: prevalence of oxygen reduction reaction and oxygen-induced amine degradation[35]. After 5 days under oxygen-rich conditions, degradation markers, such as formate and nitrite were detected in aqueous MEA but not in DMSO (Supplementary Table 3). Evaporate losses in DMSO were also less than half those observed in water.

Regarding the electrochemical performance at HOC, the porous Zn electrode reaches 80 mA cm^{-2} at −2.2 V versus $Me_{10}Fc$ at room temperature (Fig. 6b). Operation at higher current densities is constrained by a ~6 V cell voltage (Supplementary Fig. 22), reflecting the lower conductivity of non-aqueous electrolytes[17,36]. We then increased temperature to close to MEA scrubbing conditions[37] to reduce electrolyte resistance (Supplementary Table 4). At 30 °C and 40 °C, current densities increased to 100 mA cm^{-2} and 120 mA cm^{-2}, respectively, at the same voltage cut-off. Despite the HOC, DMSO electrolyte maintains substantial CO selectivity. Figure 6c shows stable CO FE between 30% and 40% across 20–40 °C and 50–100 mA cm^{-2}. With pure CO_2 feed, CO FE reaches ~85% and partial current densities up to 170 mA cm^{-2} (Supplementary Fig. 23). Since experiments were conducted in an H-cell with ~6-cm electrode spacing (Supplementary Fig. 24), compact architectures should further reduce resistance and enhance performance.

While the cathodic reactions consist mostly of amine–CO_2 reduction and HER, the anodic process remains unclear and probably involves either oxygen evolution from residual water (Supplementary Table 5) or undesired oxidation reactions. To improve electrolyte stability and ensure proton availability for CO formation, we explored hydrogen oxidation reaction (HOR) as an anodic reaction, as illustrated in Supplementary Fig. 25a. To mitigate the challenges associated with low H_2 solubility, we use a porous palladium counter electrode[38] (Supplementary Fig. 25b), which exhibits superior activity for HOR and may effectively sustain high current densities (for example, 100 mA cm^{-2}) at lower overpotential. As shown in Fig. 6d, the addition of H_2 reduces the cell overpotential up to 1.1 V, driven by a more thermodynamically favourable HOR. Cell voltage without infrared correction can be found in Supplementary Fig. 25b. No differences in the cathodic product distribution were also observed (Supplementary Fig. 24c). However, gas chromatography coupled with mass spectrometry (GC–MS) analysis shown in Fig. 6e revealed the presence of pyrazine and dimethyl sulfone for the air purge anolyte. These side products are associated with the oxidation of MEA[39] and DMSO[40], respectively. The absence of substantial amounts of these or any new side products (Supplementary Fig. 26) in the presence of H_2 highlights HOR as a possible anodic reaction for amine–CO_2 reduction in non-aqueous media.

Finally, we performed an accelerated cycling test on CO_2 capture and conversion under HOC to evaluate the electrolyte's recyclability. The solution was first saturated with HOC-FG and then purged with synthetic air (20% O_2, 80% N_2) to accelerate CO_2 displacement from the amine–CO_2 adduct. As shown in Fig. 6f, the initial CO FE reached ~43% in the HOC-FG-saturated solution. Even as the CO_2 content dropped to 3%, the system maintained a CO FE of ~20%. Some fracturing of the Zn nanoparticles and microparticles was also observed (Supplementary Fig. 21h–j). This electrode restructuring may account for the decrease in peak CO FE over the recycling cycles. Despite these structural changes, the system demonstrated stable performance during 20 recycling tests.

The use of a non-aqueous electrolyte enables integrated CO_2 capture and conversion with substantial CO formation from industrially relevant streams compositions. Figure 7 summarizes the performance of MEA-based RCC systems at ambient pressure and temperature (literature data in Supplementary Table 6). Compared with state-of-the-art aqueous reactive capture systems[6], which report ~40% CO FE over Ag under pure CO_2, we achieve up to 43% CO FE over a Zn catalyst at HOC-FG conditions. For processes supplying pure CO_2, such as ethanol or ammonia production[2], we may expect CO FE up to 80% over an earth-abundant catalyst.

Conclusions

In this study, we integrated CO_2 capture and electrochemical conversion in a non-aqueous electrolyte. Shifting amine–CO_2 speciation from carbamate to carbamic acid increases CO_2 loading threefold when moving from water to DMSO, enhancing CO_2 reduction activity and selectivity and enabling non-precious catalysts. DFT and electrochemical analysis show lower limiting potentials for Zn relative to Ag, consistent with improved CO formation. Our TEA indicates that the enhanced electrochemical performance of the Zn–DMSO system offsets higher solvent costs compared with aqueous systems. Under flue gas conditions, we achieve CO Faradaic efficiencies up to 43% at 100 mA cm^{-2} over multiple capture–conversion cycles. These results establish electrolyte-controlled speciation as a viable design strategy for selective and stable integrated CO_2 capture and conversion.

Methods

General procedures

Dimethylsulfoxide (anhydrous, 99.9%), MEA (99%) and caesium chloride (99.9%) were purchased from Sigma-Aldrich, while caesium perchlorate (99.5%) was purchased from Thermo Fisher Scientific. All other reagents were used as received, unless stated otherwise. After salt dissolution, all electrolytes presenting water content lower than 500 ppm were determined through Karl–Fischer coulometric titration. All glassware used was cleaned by first rinsing with soap and subsequently rinsing three times with each of the following solvents: ethanol (Fisher, 70%), isopropanol (StatLab, 99%) and Mili-Q water (resistivity 18.2 MΩ cm at 25 °C). Then, they were rested in a fresh acid bath containing 10% (v/v) HNO_3 solution (Fisher Chemical, TraceMetal Grade) for 24 h, rinsed again three times with Mili-Q water and dried at 80 °C for at least 6 h before use.

NMR spectroscopy characterization

d_6DMSO and D_2O were purchased from Cambridge Isotope Laboratories (99.8%). Here 10 mM tetramethylsilane (Sigma-Aldrich, 99%) was added to all samples and used as a ^{1}H NMR internal reference as 0 ppm. All ^{1}H NMR and ^{13}C NMR spectra were collected using a Bruker Ascend 9.4 T/400 MHz. For the speciation studies, ^{13}C-labelled carbon dioxide (MilliporeSigma, 99 atom% ^{13}C and 99.93 atom% ^{16}O) was purged for 30 min at 1 sccm into 0.5 ml of sample inside an NMR tube. Then, Argon (Air Gas, 99.9995%) was purged at 1 sccm for 5 min to eliminate any dissolved CO_2. Relaxation time (T1) was set to 40 s for the collection of ^{13}C NMR spectra.

Conductivity and pH measurements

Conductivity measurements were taken in a Vernier platinum-cell conductivity probe with an epoxy body. pH measurements were taken with a Mettler-Toledo SevenCompact pH meter with a pH probe Sensor InLab Smart Pro-ISM with Xerolyt polymer as a reference electrolyte and had an open junction to prevent clogging and contamination with the non-aqueous electrolytes. pH measurements taken in a non-aqueous medium were reported as apparent pH (pH_{app}).

Electrode preparation

Zinc (3.18 mm diameter, 99.994% metals basis, Thermo Scientific) and silver (3.175 mm diameter, 99.9% metals basis, Thermo Scientific) electrodes were prepared by inserting the rods in a polyether-ether-ketone (PEEK) tube. Disc electrodes were first rinsed with ethanol, isopropanol and Mili-Q water, and then intensely polished with alumina slurry to remove any superficial oxide layer before each experiment. The excess alumina slurry was removed by rinsing the electrode with Mili-Q water and using a high-pressure N_2 blow at the electrode surface. Platinum wires (25 cm long, 0.25 mm diameter, 99.9% metals basis, Thermo Scientific) were flame touched, stored in 10% HNO_3 for 24 h, rinsed with Mili-Q water and dried at 80 °C before use. Zn cloth was prepared by electrodepositing a solution of 0.1 M $ZnSO_4$ 20 g l^{-1} HBO_3 at 60 °C over a stainless-steel cloth (McMaster Carr, mesh size 400 × 400, opening size 0.00381 mm and wire diameter of 0.0254 mm) for 1 h under continuous stirring at −0.6 V versus Zn/Zn^{2+} on each side facing the counter electrode. A Zn foil (99.9% metals basis, Thermo Scientific) of equivalent size was used as a counter electrode in an two electrode cell setup. The stainless-steel cloth was first cleaned by immersing it in H_3PO_4 30% v/v for 30 min. The high surface porous palladium membranes were prepared by electrodepositing a solution of 15.6 mM $PdCl_2$ in 1 M HCl over a Pd metallic membrane (2.5 × 2.5 cm, 0.025 mm thick, 99.9% metals basis, Thermo Scientific) at −3.5 mA cm^{-2} and a total charge of 12 C cm^{-2} on each side facing the counter electrode[41]. Pt wire and Ag/AgCl were used as counter and reference electrodes, respectively.

Electrochemical measurements

Electrochemical data were acquired using a Biologic VSP potentiostat. A platinum wire (surface area of approximately 4 cm^2) was used as a counter electrode, if not stated otherwise. An Ag/AgCl leakless electrode (eDAQ, PEEK tube) was used as a pseudo reference electrode calibrated against either the reversible hydrogen (following the procedures further described in Supplementary Note 1) or 3 mM $Me_{10}Fc$ using a glassy carbon working electrode (eDAQ) after each experiment. The uncompensated resistance (R_u) was acquired at −1.0 versus Ag/AgCl at the high-frequency regime of the electrochemical impedance spectra (100 kHz). All potentials were reported after 100% manual after-the-scan infrared compensation using the average R_u value for each electrolyte.

Product distribution analysis

Production distribution analysis was performed using a Biologic VSP potentiostat with a glass H-cell illustrated in Supplementary Fig. 23. Both catholyte and anolyte chambers were filled with the same solutions, which were separated by a Nafion-N117 (Alfa-Aesar) proton exchange membrane. A stir bar at 900 rpm was kept going on both chambers. Vigorous stirring was needed to remove bubbles formed on the electrode surface. Three gas flow controllers (Alicat Scientific) were connected in parallel to a gas mixer and then aligned to the catholyte chamber of the H-cell. CO_2 (99.9995%), N_2 (99.9995%), synthetic air (20% O_2 and 80% N_2, 99.999%) and Ar (99.9995%) were all purchased from Airgas. H_2 (99.9%) was supplied by a portable hydrogen generator (Hydrofill Pro, Horizon Education). Products in the gas phase were analysed in-line using a CO_2 sensor (SprintIR-W 100%, CO2Meter) and Shimadzu GC-2014 gas chromatograph with both a flame ionization detector and a thermal conductive detector. Current values were averaged for 1 min before each injection. Products in the liquid phase were analysed using ^{1}H NMR in a Bruker Ascend 9.4 T/400 MHz instrument or had their headspace analysed at 120 °C using a gas chromatograph coupled with a mass spectrometer (GC–MS-QP2020 NX Single Quadrupole, Shimadzu).

CO_2 displacement test

The CO_2 displacement test was performed in an air-tight cell as illustrated in Supplementary Fig. 7a. The cell compartment had a total volume of 15 ml. Then 10 ml of the CO_2-saturated sample was stirred at 750 rpm while being purged with Ar at 10 sccm. An ExplorIR-M 100% CO_2 Sensor (CO2meter) was used to monitor the cell headspace outlet. The cell pressure was kept near 1 atm.

Expedited amine loss and degradation test

Solutions of 1 M MEA in either water or DMSO were kept at 50 °C in an air-tight cell and stirred at 750 rpm while being purged with air at 20 sccm for 5 days. Products in the liquid phase were quantified at the end of the fifth day by using ion chromatography (LC-20Ai IC, Shimadzu) consisting of a conductivity detector (CDD-10AVP) and an analytical column (Shodex IC NI-424, anion-specific) coupled with a guard column (Shodex IC IA-G). The column was maintained at 40 °C, while the mobile phase consisted of 8 mM 4-hydroxybenzoic acid, 1.9 mM Bis-Tris, 2 mM phenylboronic acid and 0.005 mM *trans*-1, 2-diaminocyclohexane-*N*,*N*,*N*′,*N*′-tetraacetic acid in aqueous solution

DFT calculations

DFT calculations with periodic boundaries were carried out using the plane-wave-based Vienna ab initio Simulation Package[42–45]. The projector augmented wave method[46] was used to describe the ionic cores; the generalized gradient approximation PBE functional[47] was used to account for the exchange–correlation effects in the Kohn–Sham framework. The bulk structure of Ag and Zn were optimized using 520 eV of cut-off energy and an 8 × 8 × 8 *k*-point mesh based on the Monkhorst–Pack scheme. The Ag (111) and Zn (101) facets were cleaved from the optimized bulk. Further details about surface calculations, box size, number of molecules, ionic relaxation and reaction coordinates are further described in Supplementary Note 3.

TEA

The TEA was based on the process for integrated carbon capture and electrochemical conversion, further described in Supplementary Note 3. The process model included a physics-based, 0-D model of the electrochemical cell to model CO reduction, and a flash column to model the vapour–liquid phase equilibrium to account for solvent and amine loss into the vapour-phase stream. The outlet stream from the capture unit (comprising solvent, amine, salt and captured CO_2) constituted the feed stream into the electrochemical cell. Product recovery was by phase separation as no liquid products were formed, and the regenerated amine stream was recycled back into the capture unit. Amine make-up was included to account for amine and solvent loss. A purge was added to account for water treatment. Model inputs included economic data such as material and electricity costs, and

experimental data such as amine–CO_2 uptake, FE and total current density measured at different potentials, corresponding component molar fractions in the liquid and vapour phase of the electrochemical cell outlet stream, and carbonate loss. Key model outputs included energy and conversion efficiency, overpotentials, overall reaction rates, outlet and/or product stream compositions and molar flow rates, energy demand, system size, material quantities, capital costs (for example, anode, cathode, membrane and cell material costs) and operating costs (for example, electricity, maintenance and make-up costs). Details of the TEA model are included in Supplementary Note 2.

Data availability

The authors declare that all data supporting the findings of this study are provided within the article and Supplementary Information. DFT optimized structures and TEA inputs underlying the computational, thermodynamic and cost modelling results are publicly available via GitHub at https://github.com/AmanchukwuLab/reactive-co2-capture-nonaqueous-electrolyte (ref. 48). Source data are provided with this paper.

Code availability

All scripts used to generate the TEA figures, heatmaps, sensitivity analyses and associated input datasets are publicly available via GitHub at https://github.com/AmanchukwuLab/reactive-co2-capture-nonaqueous-electrolyte (ref. 42).

References

1. Sullivan, I. et al. Coupling electrochemical CO_2 conversion with CO_2 capture. *Nat. Catal.* **4**, 952–958 (2021).
2. Morgan Summers, W., Herron, S. E. & Zoelle, A. *Cost of Capturing CO_2 from Industrial Sources* (National Energy Technology Laboratory, Office of Fossil Energy, 2014).
3. Boot-Handford, M. E. et al. Carbon capture and storage update. *Energy Environ. Sci.* **7**, 130–189 (2013).
4. Kim, Y. et al. Economic viability of Integrated CO_2 capture and conversion. *ACS Energy Lett.* **10**, 403–409 (2024).
5. Banerjee, A. & Morales-Guio, C. G. Integrated CO_2 capture and electrochemical conversion: coupled effects of transport, kinetics and thermodynamics in the direct reduction of captured-CO_2 adducts. *EES Catal.* **3**, 205–234 (2025).
6. Lee, G. et al. Electrochemical upgrade of CO_2 from amine capture solution. *Nat. Energy* **6**, 46–53 (2021).
7. Jerng, S. E. & Gallant, B. M. Electrochemical reduction of CO_2 in the captured state using aqueous or nonaqueous amines. *iScience* **25**, 104558 (2022).
8. Kortunov, P. V., Siskin, M., Baugh, L. S. & Calabro, D. C. In situ nuclear magnetic resonance mechanistic studies of carbon dioxide reactions with liquid amines in aqueous systems: new insights on carbon capture reaction pathways. *Energy Fuels* **29**, 5919–5939 (2015).
9. Shen, K. et al. On the origin of carbon sources in the electrochemical upgrade of CO_2 from carbon capture solutions. *Joule* **7**, 1260–1276 (2023).
10. Safipour, J., Weber, A. Z. & Bell, A. T. Detrimental effects of monoethanolamine and other amine-based capture agents on the electrochemical reduction of CO_2. *ACS Energy Lett.* **8**, 5012–5017 (2023).
11. Wang, M. et al. Acidic media enables oxygen-tolerant electrosynthesis of multicarbon products from simulated flue gas. *Nat. Commun.* **15**, 1218 (2024).
12. Li, P. et al. Acid–base interaction enhancing oxygen tolerance in electrocatalytic carbon dioxide reduction. *Angew. Chem. Int. Ed.* **59**, 10918–10923 (2020).
13. Xu, Y. et al. Oxygen-tolerant electroproduction of C_2 products from simulated flue gas. *Energy Environ. Sci.* **13**, 554–561 (2020).
14. Leverick, G. et al. Uncovering the active species in amine-mediated CO_2 reduction to CO on Ag. *ACS Catal.* **13**, 12322–12337 (2023).
15. Bhattacharya, M., Sebghati, S., Vercella, Y. M. & Saouma, C. T. Electrochemical reduction of carbamates and carbamic acids: implications for combined carbon capture and electrochemical CO_2 recycling. *J. Electrochem. Soc.* **167**, 086507 (2020).
16. Pérez-Gallent, E., Vankani, C., Sánchez-Martínez, C., Anastasopol, A. & Goetheer, E. Integrating CO_2 capture with electrochemical conversion using amine-based capture solvents as electrolytes. *Ind. Eng. Chem. Res.* **60**, 4269–4278 (2021).
17. Gomes, R. J. et al. Modulating water hydrogen bonding within a non-aqueous environment controls its reactivity in electrochemical transformations. *Nat. Catal.* **7**, 689–701 (2024).
18. Kortunov, P. V., Siskin, M., Baugh, L. S. & Calabro, D. C. In situ nuclear magnetic resonance mechanistic studies of carbon dioxide reactions with liquid amines in non-aqueous systems: evidence for the formation of carbamic acids and zwitterionic species. *Energy Fuels* **29**, 5940–5966 (2015).
19. Chu, A. T., Jung, O., Toh, W. L. & Surendranath, Y. Organic non-nucleophilic electrolyte resists carbonation during selective CO_2 electroreduction. *J. Am. Chem. Soc.* https://doi.org/10.1021/JACS.3C00506 (2023).
20. Szwabińska, K. & Lota, G. Tuning the course of the oxygen reduction reaction at a carbon electrode using alkaline electrolytes based on binary DMSO–water solvent mixtures. *Electrochem. Commun.* **141**, 107359 (2022).
21. Khurram, A., Yan, L., Yin, Y., Zhao, L. & Gallant, B. M. Promoting amine-activated electrochemical CO_2 conversion with alkali salts. *J. Phys. Chem. C.* **123**, 18222–18231 (2019).
22. Kuo, F. Y., Jerng, S. E. & Gallant, B. M. Dual salt cation-swing process for electrochemical CO_2 separation. *ACS Cent. Sci.* **9**, 1750–1757 (2023).
23. Dijkstra, Z. J. et al. Formation of carbamic acid in organic solvents and in supercritical carbon dioxide. *J. Supercrit. Fluids* **41**, 109–114 (2007).
24. Kash, B., Gomes, R. & Amanchukwu, C. Mitigating electrode inactivation during CO_2 electrocatalysis in aprotic solvents with alkali cations. *J. Phys. Chem. Lett.* **14**, 920–926.
25. Niu, S., Li, S., Du, Y., Han, X. & Xu, P. How to reliably report the overpotential of an electrocatalyst. *ACS Energy Lett.* **5**, 1083–1087 (2020).
26. Won, D. H. et al. Highly efficient, selective, and stable CO_2 electroreduction on a hexagonal Zn catalyst. *Angew. Chem.* **128**, 9443–9446 (2016).
27. Rosen, J. et al. Electrodeposited Zn dendrites with enhanced CO selectivity for electrocatalytic CO_2 reduction. *ACS Catal.* **5**, 4586–4591 (2015).
28. Ikeda, S., Takagi, T. & Ito, K. Selective formation of formic acid, oxalic acid, and carbon monoxide by electrochemical reduction of carbon dioxide. *Bull. Chem. Soc. Jpn* **60**, 2517–2522 (1987).
29. Bagger, A., Christensen, O., Ivaništšev, V. & Rossmeisl, J. Catalytic CO_2/CO reduction: gas, aqueous, and aprotic phases. *ACS Catal.* **12**, 2561–2568 (2022).
30. Welford, P. J. et al. The electro-reduction of carbon dioxide in dimethyl sulfoxide at gold microdisk electrodes: current | voltage waveshape analysis. *J. Phys. Chem. B* **105**, 5253–5261 (2001).
31. Gomes, R. J. et al. Probing electrolyte influence on CO_2 reduction in aprotic solvents. *J. Phys. Chem. C.* **126**, 13595–13606 (2022).
32. Khurram, A., He, M. & Gallant, B. M. Tailoring the discharge reaction in Li-CO_2 batteries through incorporation of CO_2 capture chemistry. *Joule* **2**, 2649–2666 (2018).
33. Xiao, Y. C. et al. Reactive capture of CO_2 via amino acid. *Nat. Commun.* **15**, 7849 (2024).

34. Lu, Q. et al. A selective and efficient electrocatalyst for carbon dioxide reduction. *Nat. Commun.* **5**, 3242 (2014).
35. Barlow, J. M. & Yang, J. Y. Oxygen-stable electrochemical CO_2 capture and concentration with quinones using alcohol additives. *J. Am. Chem. Soc.* **144**, 14161–14169 (2022).
36. Lazouski, N., Chung, M., Williams, K., Gala, M. L. & Manthiram, K. Non-aqueous gas diffusion electrodes for rapid ammonia synthesis from nitrogen and water-splitting-derived hydrogen. *Nat. Catal.* **3**, 463–469 (2020).
37. Alie, C., Backham, L., Croiset, E. & Douglas, P. L. Simulation of CO_2 capture using MEA scrubbing: a flowsheet decomposition method. *Energy Convers. Manag.* **46**, 475–487 (2005).
38. Omasta, T. J. et al. Beyond 1.0 W cm^{-2} performance without platinum: the beginning of a new era in anion exchange membrane fuel cells. *J. Electrochem. Soc.* **165**, J3039–J3044 (2018).
39. Rey, A. et al. Amine degradation in CO_2 capture. 2. New degradation products of MEA. Pyrazine and alkylpyrazines: analysis, mechanism of formation and toxicity. *Int. J. Greenh. Gas. Control* **19**, 576–583 (2013).
40. Sharon, D. et al. Oxidation of dimethyl sulfoxide solutions by electrochemical reduction of oxygen. *J. Phys. Chem. Lett.* **4**, 3115–3119 (2013).
41. Delima, R. S., Sherbo, R. S., Dvorak, D. J., Kurimoto, A. & Berlinguette, C. P. Supported palladium membrane reactor architecture for electrocatalytic hydrogenation. *J. Mater. Chem. A Mater.* **7**, 26586–26595 (2019).
42. Kresse, G. & Joubert, D. From ultrasoft pseudopotentials to the projector augmented-wave method. *Phys. Rev. B* **59**, 1758 (1999).
43. Kresse, G. & Furthmüller, J. Efficient iterative schemes for ab initio total-energy calculations using a plane-wave basis set. *Phys. Rev. B* **54**, 11169 (1996).
44. Kresse, G. & Furthmüller, J. Efficiency of ab-initio total energy calculations for metals and semiconductors using a plane-wave basis set. *Comput. Mater. Sci.* **6**, 15–50 (1996).
45. Kresse, G. & Hafner, J. Ab initio molecular dynamics for liquid metals. *Phys. Rev. B* **47**, 558 (1993).
46. Blöchl, P. E. Projector augmented-wave method. *Phys. Rev. B* **50**, 17953 (1994).
47. Perdew, J. P., Burke, K. & Ernzerhof, M. Generalized gradient approximation made simple. *Phys. Rev. Lett.* **77**, 3865 (1996).
48. Repository for DFT optimized structures and techno economic analysis workflows supporting reactive CO_2 capture in nonaqueous electrolytes. *GitHub* https://github.com/AmanchukwuLab/reactive-co2-capture-nonaqueous-electrolyte

Acknowledgements

This work was primarily supported by the University of Chicago Joint Task Force Initiative and the US Department of Energy, Office of Science Basic Energy Sciences, Early Career Research Program (grant no. DE-SC0024103). Argonne National Laboratory's work was supported by the US Department of Energy, Office of Energy Efficiency and Renewable Energy, Industrial Efficiency and Decarbonization Office under contract no. DE-AC02-06CH11357. C.V.A. was supported by the CIFAR Azrieli Global Scholars Program and the Research Corporation for Science Advancement Negative Emissions Science programme (through the Alfred P. Sloan Foundation, grant no. G-2023-19630). R.J.G. was partially supported by the Roberto Rocca Fellowship Program. We thank C. Vu and H. Srinivasan for collecting the X-ray diffraction data. This work made use of the shared facilities (X-ray diffraction) at the University of Chicago Materials Research Science and Engineering Center, supported by the National Science Foundation under award number DMR-2011854. Solution-state NMR measurements were performed at the UChicago Chemistry NMR Facility. This work has been supported by UChicago Argonne LLC, Operator of Argonne National Laboratory ('Argonne'). Argonne, a US Department of Energy Office of Science laboratory, is operated under contract no. DE-AC02-06CH11357. The US Government retains for itself, and others acting on its behalf, a paid-up nonexclusive, irrevocable worldwide license in said article to reproduce, prepare derivative works, distribute copies to the public and perform publicly and display publicly, by or on behalf of the Government. The Department of Energy will provide public access to these results of federally sponsored research in accordance with the DOE Public Access Plan.

Author contributions

R.J.G., C.L., C.O.I. and C.V.A. conceptualized the paper. R.J.G. designed and performed the experimental investigation with B.S., M.M. and I.R. assisting with NMR, scanning electron microscopy, degradation studies and product distribution analysis. J.X. and J.G. carried out the DFT calculations with supervision from C.L. J.L. and T.M. carried out the TEA analysis with supervision from C.O.I. N.P participated in discussions and revised the paper. R.J.G. and C.V.A. wrote the paper and all authors contributed to discussions and editing. C.V.A. supervised the work.

Competing interests

The authors declare that a patent application related to this work has been filed. R.J.G. and C.V.A. are named as inventors of this application. The other authors declare no competing interests.

Additional information

Supplementary information The online version contains supplementary material available at https://doi.org/10.1038/s41560-026-02035-4.

Correspondence and requests for materials should be addressed to Chibueze V. Amanchukwu.

Peer review information *Nature Energy* thanks Michal Bajdich, Geonhui Lee and the other, anonymous, reviewer(s) for their contribution to the peer review of this work.

QUERY FORM

Manuscript ID	**[Art. Id: 2035]**
Author	**Reginaldo J. Gomes**

AUTHOR:

The following queries have arisen during the editing of your manuscript. Please answer by making the requisite corrections directly in the e.proofing tool rather than marking them up on the PDF. This will ensure that your corrections are incorporated accurately and that your paper is published as quickly as possible.

Query No.	*Nature of Query*
Q1:	Please confirm or correct the country name inserted in affiliation 1-5.
Q2:	Please check your article carefully, coordinate with any co-authors and enter all final edits clearly in the eproof, remembering to save frequently. Once corrections are submitted, we cannot routinely make further changes to the article.
Q3:	Note that the eproof should be amended in only one browser window at any one time; otherwise changes will be overwritten.
Q4:	Author surnames have been highlighted. Please check these carefully and adjust if the first name or surname is marked up incorrectly, as this will affect indexing of your article in public repositories such as PubMed. Also, carefully check the spelling and numbering of all author names and affiliations, and the corresponding author(s) email address(es). Please note that email addresses should only be included for designated corresponding authors, and you cannot change corresponding authors at this stage except to correct errors made during typesetting.
Q5:	You cannot alter accepted Supplementary Information files except for critical changes to scientific content. If you do resupply any files, please also provide a brief (but complete) list of changes. If these are not considered scientific changes, any altered Supplementary files will not be used, only the originally accepted version will be published.
Q6:	Please check Figures for accuracy as they have been relabelled. Please markup minor changes in the eProof. For major changes, please provide revised figures. (Please note that in the eProof the figure resolution will appear at lower resolution than in the pdf and html versions of your paper.)
Q7:	If applicable, please ensure that any accession codes and datasets whose DOIs or other identifiers are mentioned in the paper are scheduled for public release as soon as possible, we recommend within a few days of submitting your proof, and update the database record with publication details from this article once available.
Q8:	In the fig. 2 caption please define LTOC and LTVOM.
Q9:	In the sentence beginning 'In contrast, Fig. 2f shows ...' please define j_{CO}

QUERY FORM

Manuscript ID	**[Art. Id: 2035]**
Author	**Reginaldo J. Gomes**

AUTHOR:

The following queries have arisen during the editing of your manuscript. Please answer by making the requisite corrections directly in the e.proofing tool rather than marking them up on the PDF. This will ensure that your corrections are incorporated accurately and that your paper is published as quickly as possible.

Query No.	*Nature of Query*
Q10:	Please check the definitions for Cdl and j added in the figure 4 caption are correct.
Q11:	Please check the link https://github.com/AmanchukwuLab/reactive-co2-capture-nonaqueous-electrolyte as it does not work. Please amend.
Q12:	Please check the updated article number in ref. 11
Q13:	please check the updated publication details in refs. 17 and 33.
Q14:	In ref. 24 please provide the publication date.
Q15:	Please update the link and add the author name(s) and date to ref. 48.